

Microscopic investigation of magnetic and antimagnetic rotational motion in atomic nuclei

W. Tawseef,¹ Nazira Nazir,^{1,*} S. Jehangir,^{2,†} J. A. Sheikh,^{1,‡} C. Majumder,³ S. Chakraborty,⁴ G. B. Vakil,¹ G. H. Bhat,⁵ and N. A. Rather⁶

¹*Department of Physics, University of Kashmir, Srinagar, Jammu and Kashmir, 190 006, India*

²*Department of Physics, Govt. Degree College Kulgam, Jammu and Kashmir, 192231, India*

³*Department of Physics, Indian Institute of Technology Bombay, Mumbai, 400076, India*

⁴*Institute of Engineering & Management, University of Engineering and Management, Kolkata, 700091, India*

⁵*Department of Physics, GDC Shopian, Higher Education, Jammu and Kashmir, 192 303, India*

⁶*Department of Physics, Islamic University of Science and Technology, Jammu and Kashmir, 192 122, India*

(Dated: January 21, 2026)

In the present work, we have generalized the projected shell model (PSM) approach to include the quasiparticle excitations from two major oscillator shells, and have also extended the basis space to five-quasiparticle configurations for odd-mass nuclei. The magnetic and antimagnetic rotational structures observed in odd-neutron Pd- and Cd-isotopes have been investigated as a first major application of the new development. It is shown that PSM approach provides a reasonable description of the observed properties of magnetic and antimagnetic rotational bands.

I. INTRODUCTION

Atomic nucleus is among a few quantum many-body systems that displays a rich diversity of excitation modes which include rotational, vibrational and single-particle mechanisms [1, 2]. The nuclei in the vicinity of the spherical shell closures, generally, depict single-particle and vibrational excitation modes in the low-spin region, and nuclei far from closed shells exhibit rotational motion. The rotational spectra have the characteristic feature of strong electric quadrupole transitions and can be understood by considering the collective motion of all the nucleons in the nucleus. In the mean-field approach, a deformed potential with ellipsoidal shape describes the observed strong quadrupole transitions [1]. The deformed potential defines the orientation with respect to the space fixed axis in an analogous manner to the diatomic molecules. In most of the nuclei, the band structures can be generated by considering rotation about an axis perpendicular to the symmetry axis of the spheroidal potential. This geometry leads to the signature quantum number with dominant quadrupole transitions along each signature branch [3, 4].

The above simple picture of the nuclear excitation modes prevailed until a new class of band structures were discovered in the vicinity of the closed shell structures [5, 6]. It was observed that nuclei with a few proton holes and neutron particles in the Pb-region have rotational like band structures with magnetic dipole B(M1) transitions dominating rather than electric quadrupole B(E2) transitions [7]. These nuclei have very small deformation and the rotational collective motion of a deformed system can be ruled out. The new band structures were interpreted [7–10] in terms of “shears” mechanism with proton holes and neutron particles forming two blades of a pair of shears. The angular-momentum of the proton holes, occupying high-K orbitals, is oriented towards the

symmetry axis, whereas the angular-momentum of the neutron particles, filling low-K orbitals, is aligned towards an axis perpendicular to the symmetry axis. The high-spin states are then generated by closing the blades of shears with the highest angular-momentum obtained when the proton and neutron vectors coincide. The perpendicular components of the neutron and proton dipole moments add up at the band head that results into a large B(M1) transition. However, the closing of the blades with increasing spin leads to decrease in the dipole moment and consequently the B(M1) transitions are also reduced with spin. The reduction of the B(M1) transitions have been observed in many systems and affirms the shears mechanism interpretation of the rotational like band structures observed in the vicinity of the closed shells [6, 8, 11–13]. The name magnetic rotation (MR) has been ascribed to this new phenomenon as it is the rotation of the magnetic dipole vector in space that is responsible in generating the band structures.

It was predicted, soon after the MR bands were discovered, that it should be also possible to observe the antimagnetic rotation (AMR) phenomenon [3, 4, 14–18]. In this alternative geometry, two neutron-proton pairs form subsystems of two shears with the magnetic dipole vectors of the shears anti-aligned. This arrangement has net zero dipole moment and is quite similar to anti-ferromagnetism in condensed matter physics. In an antiferromagnetic material, one-half of the dipole moments in one sublattice is aligned in one direction and the other half is oriented in the opposite direction in the second sublattice with net zero total dipole moment. At the band head, the angular momentum of the proton holes is aligned towards the opposite sides of the symmetry axis, and angular-momentum of the neutron particles is directed along the rotational axis. The AMR band is generating by simultaneously moving the two proton blades towards the angular-momentum vector of the neutrons.

There are two characteristics features of the AMR phenomenon, one is the absence of the B(M1) transitions as the magnetic dipoles of the two shears are anti-aligned. The second is that the system in the AMR configuration is symmetric with respect to rotation by π about the total angular-momentum axis. This corresponds to the signature symme-

* naziranazir238@gmail.com

† sheikhahmad.phy@gmail.com

‡ sjaphysics@gmail.com

try and the AMR band should consist of regular sequence of energy levels differing in spin by $2\hbar$. The in-band E2 cascades should be weak considering that AMR configurations are weakly deformed.

The MR structures have been observed in several regions of the Segre chart and 225 bands observed in 114 nuclides are tabulated in Ref. [19]. The AMR, on the other hand, is a subtle phenomenon and, so far, 37 such band structures have been reported in 27 nuclei [19]. It was predicted [3, 4] as a alternative mechanism of generating angular-momentum and should occur in the same regions where the MR mode have been observed. Nuclei in the $A \sim 110$ region, in particular the Cadmium isotopes, were proposed to be the ideal candidates to explore the AMR mode [20, 21]. Cadmium has two proton holes in high- Ω orbitals in $1h_{9/2}$ subshell that will couple with neutrons in low- Ω orbitals $1h_{11/2}$ to form the twin-shears configuration of the AMR mode. As a matter of fact, the first AMR band structure was identified in ^{109}Cd [21, 22] with lifetime measurements clearly demonstrating a decreasing trend in the B(E2) values with increasing spin, and the ratio of the moment of inertia to B(E2) of about $165 \hbar^2 \text{ MeV}^{-1} (\text{eb})^{-2}$. AMR band structures have been reported in other nuclei, in particular, detailed investigations have been performed for ^{101}Pd [23–25], ^{103}Pd [26], ^{105}Cd [27] and ^{107}Cd [28] nuclides.

Theoretically, several models have been proposed to elucidate the properties of MR and AMR band structures. These include cranked shell model (CSM) [9], semiclassical model (SCM) [21–24] and relativistic density functional theory (RDFT) approaches [16, 29]. The CSM approach, as a matter of fact, was originally used to predict the existence of the AMR mode [14]. The SCM approach is a semiclassical version of the particle-rotor model with predefined shears arrangement for the valence nucleons. This model has been shown to provide a good description of the properties of AMR bands. RDFT model has been used to investigate the high-spin properties of ^{105}Cd and it has been shown that polarization effects play an important role to describe the AMR features.

In the present work, we have developed an alternative approach of the projected shell model (PSM) to investigate the properties of the AMR and MR band structures. In the PSM approach, the angular-momentum projection is carried out, and the wavefunctions have well defined angular-momentum. In comparison to the cranking approximation employed in the other models, the PSM approach is well suited to study the electromagnetic transition probabilities. In the earlier version of the PSM approach, the valence particles were restricted to one major oscillator shell [30–33]. In the present work, we have extended the model space and the valence nucleons can occupy two major oscillator shells. Further, we have also generalized the PSM approach to include up to five quasiparticle configurations in odd-mass nuclei. This extension, as will be discussed in the next section, is needed to explore the properties of the MR and AMR bands observed in $A \sim 110$ region. The manuscript is organised in the following manner. In the next section, the extended PSM approach is presented with a focus on odd-neutron systems. We have also employed the semiclassical particle rotor model to obtain the properties of

the Pd- and Cd- nuclides as an alternative approach. Although this approach is well documented [34–36], but for completeness, we shall briefly discuss it in section III. In section IV, the results obtained on excitation energies, alignments and transition probabilities for chains of odd-neutron Cadmium and Palladium nuclides are presented and discussed. Finally, the present work is summarized and concluded in section V.

II. EXTENDED PSM APPROACH

In the present work, we have considerably extended the basis space in the PSM approach, and the complete set of configurations is given by :

$$\begin{aligned} & \hat{P}_{MK}^I a_{v_1}^\dagger | \Phi \rangle; \\ & \hat{P}_{MK}^I a_{v_1}^\dagger a_{\pi_1}^\dagger a_{\pi_2}^\dagger | \Phi \rangle; \\ & \hat{P}_{MK}^I a_{v_1}^\dagger a_{v_2}^\dagger a_{v_3}^\dagger | \Phi \rangle; \\ & \hat{P}_{MK}^I a_{v_1}^\dagger a_{v_2}^\dagger a_{v_3}^\dagger | \Phi \rangle; \\ & \hat{P}_{MK}^I a_{v_1}^\dagger a_{v_2}^\dagger a_{v_3}^\dagger a_{\pi_1}^\dagger a_{\pi_2}^\dagger | \Phi \rangle; \\ & \hat{P}_{MK}^I a_{v_1}^\dagger a_{v_2}^\dagger a_{v_3}^\dagger a_{\pi_1}^\dagger a_{\pi_2}^\dagger | \Phi \rangle, \end{aligned} \quad (1)$$

where $|\Phi\rangle$ is the deformed quasiparticle vacuum state, and \hat{P}_{MK}^I is the angular-momentum-projection operator given by [2] :

$$\hat{P}_{MK}^I = \frac{2I+1}{8\pi^2} \int d\Omega D_{MK}^I(\Omega) \hat{R}(\Omega), \quad (2)$$

with the rotation operator

$$\hat{R}(\Omega) = e^{-i\alpha\hat{J}_z} e^{-i\beta\hat{J}_y} e^{-i\gamma\hat{J}_z}. \quad (3)$$

Here, "Ω" represents the set of Euler angles ($\alpha, \gamma = [0, 2\pi]$, $\beta = [0, \pi]$). In the present work axial symmetry has been assumed and the basis configurations in Eq. (1) have well defined "K" (projection of the angular-momentum along the symmetry axis) value. This symmetry has been imposed as magnetic and antimagnetic rotational bands are considered to preserve the axial symmetry. The advantage is that the three-dimensional integration reduces to only one as the intrinsic state is an eigenstate of the \hat{J}_z operator.

In Eq. (1), v and v' denote the quantities in two different oscillator shells. For instance, in the mass $A \sim 110$ region, neutrons (protons) occupy $N = 3, 4, 5$ (2, 3, 4) shells, the index v and v' represent neutrons occupying $N = 5$ and 4 shell respectively. In the original version of the PSM program [30], particles are restricted to occupy only one major oscillator shell [30].

The above basis states are used to diagonalize the shell model Hamiltonian, given by :

$$\hat{H} = \hat{H}_0 - \frac{1}{2} \chi \sum_{\mu} \hat{Q}_{\mu}^\dagger \hat{Q}_{\mu} - G_M \hat{P}^\dagger \hat{P} - G_Q \sum_{\mu} \hat{P}_{\mu}^\dagger \hat{P}_{\mu}. \quad (4)$$

The above Hamiltonian, consisting of pairing and quadrupole-quadrupole interactions, is the same as used in all earlier PSM calculations [30]. In the above equation, \hat{H}_0 is the spherical

single-particle part of the Nilsson potential [37]. The strength parameter χ in Eq. (4) is fixed using the self-consistent condition [30].

$$\chi_{\tau\tau'} = \frac{\frac{2}{3}\varepsilon\hbar\omega_{\tau}\hbar\omega_{\tau'}}{\hbar\omega_n\langle\hat{Q}_0\rangle_n + \hbar\omega_p\langle\hat{Q}_0\rangle_p} \quad (5)$$

The above equation follows from the fact that the quadrupole term in the Nilsson model is the mean-field of quadrupole-quadrupole interaction. The pairing interaction is fitted using the parametrization

$$G_M = \left[G_1 \mp G_2 \frac{N-Z}{A} \right] \frac{1}{A} \quad (6)$$

where “+ (-)” is for protons (neutrons), and G_1 and G_2 are coupling constants which are fitted to the odd-even mass differences. The parameters are $G_1 = 22.68$ and $G_2 = 16.22$.

The electromagnetic transition probabilities from an initial state $\psi^{\sigma_i I_i}$ to a final state $\psi^{\sigma_f I_f}$ are obtained using the expression [31]:

$$B(E2, I_i \rightarrow I_f) = \frac{e^2}{2I_i + 1} |\langle \psi^{\sigma_f I_f} \parallel \hat{Q}_2 \parallel \psi^{\sigma_i I_i} \rangle|^2. \quad (7)$$

The reduced magnetic dipole transition probability $B(M1)$ is evaluated using

$$B(M1, I_i \rightarrow I_f) = \frac{\mu_N^2}{2I_i + 1} |\langle \psi^{\sigma_f I_f} \parallel \hat{\mathcal{M}}_1 \parallel \psi^{\sigma_i I_i} \rangle|^2, \quad (8)$$

where the magnetic dipole operator is defined as

$$\hat{\mathcal{M}}_1^{\tau} = g_l^{\tau} \hat{j}^{\tau} + (g_s^{\tau} - g_l^{\tau}) \hat{s}^{\tau}. \quad (9)$$

For an irreducible spherical tensor, \hat{Q} , of rank L , the reduced matrix element can be expressed as

$$\begin{aligned} \langle \psi^{\sigma_f I_f} \parallel \hat{Q}_L \parallel \psi^{\sigma_i I_i} \rangle &= \sum_{\kappa_i, \kappa_f, K_i, K_f} f_{\kappa_i K_i}^{\sigma_i I_i} f_{\kappa_f K_f}^{\sigma_f I_f} \sum_{M_i, M_f, M} (-)^{I_f - M_f} \\ &\quad \times \begin{pmatrix} I_f & L & I_i \\ -M_f & M & M_i \end{pmatrix} \\ &\quad \times \langle \Phi_{\kappa_f} | \hat{P}_{K_f M_f}^{I_f} \hat{Q}_{LM} \hat{P}_{K_i M_i}^{I_i} | \Phi_{\kappa_i} \rangle \quad (10) \\ &= 2 \sum_{\kappa_i, \kappa_f, K_i, K_f} f_{\kappa_i K_i}^{\sigma_i I_i} f_{\kappa_f K_f}^{\sigma_f I_f} \sum_{M', M''} (-)^{I_f - K_f} (2I_f + 1)^{-1} \\ &\quad \times \begin{pmatrix} I_f & L & I_i \\ -K_f & M' & M'' \end{pmatrix} \int d\Omega D_{M'' K_i}^{I_i}(\Omega) \\ &\quad \times \langle \Phi_{\kappa_f} | \hat{Q}_{LM'} \hat{R}(\Omega) | \Phi_{\kappa_i} \rangle. \end{aligned}$$

The symbol $(\)$ in the above expression represents a $3j$ -coefficient.

III. SEMICLASSICAL PARTICLE-ROTOR MODEL

The semiclassical model (SCM), originally developed by Macchiavelli *et al.* [34, 35] to describe magnetic rotation, was

TABLE I. Axial quadrupole deformation (ε) and pairing gap parameters (Δ_n and Δ_p) employed in the PSM calculation. Axial deformations ε have been considered from the refs. [20, 21, 25, 26, 38–45].

	^{101}Pd	^{103}Pd	^{107}Pd	^{109}Pd	^{111}Pd
ε	0.128 (0.165)	0.180	0.220	0.200	0.230
Δ_n	0.657	0.957	0.684	1.025	0.827
Δ_p	0.772	0.995	0.742	0.912	0.901
	^{103}Cd	^{105}Cd	^{107}Cd	^{109}Cd	^{111}Cd
ε	0.150	0.140	-0.110	0.140	0.140
Δ_n	0.568	0.586	1.142	1.125	0.992
Δ_p	0.756	0.897	0.878	0.947	0.806

later modified by Sugawara *et al.* [36] to explain antimagnetic rotational bands. In this framework, the angular momentum of the neutron particles is denoted by \vec{j}_v , while those of the two proton holes are \vec{j}_{π}^1 and \vec{j}_{π}^2 . The angle between \vec{j}_v and each proton-hole angular momentum vector is the shears angle θ . The total angular momentum is generated through the gradual closing of the two shears blades in a back-to-back symmetric fashion, as illustrated in Fig. 1. Owing to this symmetry, antimagnetic rotational bands consist of levels differing in spin by $2\hbar$.

The total energy $E(I(\theta))$ is expressed as the sum of the rotational energy of the core and the effective interaction energy between the shears blades,

$$\begin{aligned} E(I(\theta)) &= \frac{R^2}{2\mathfrak{J}^{(2)}} + V_2 P_2(\theta) \\ &= \frac{(I - j_{\pi} - j_v)^2}{2\mathfrak{J}^{(2)}} + V_2 P_2(\theta). \end{aligned} \quad (11)$$

Expanding the interaction term to include proton–neutron and

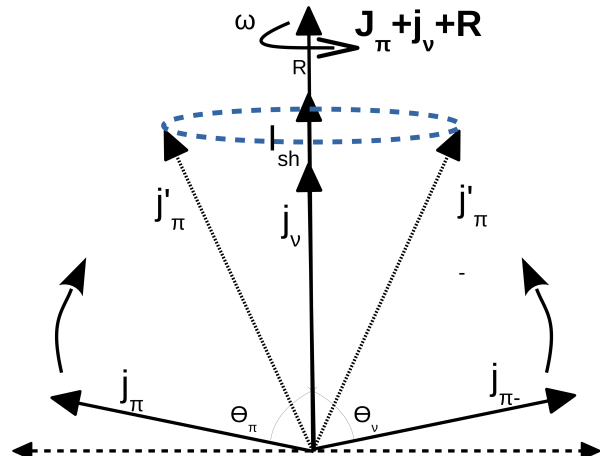


FIG. 1. Schematic illustration of the twin-shears mechanism leading to the formation of an antimagnetic rotational band.

proton–proton interactions, the total energy can be written as

$$E(I) = \frac{(I - j_\pi - j_\nu)^2}{2\mathfrak{J}^{(2)}} + \frac{V_{\pi\nu}}{2} (3 \cos^2 \theta - 1) - \frac{V_{\pi\pi}}{n} \frac{(3 \cos^2(2\theta) - 3)}{2}. \quad (12)$$

Here, $\mathfrak{J}^{(2)}$ denotes the dynamic moment of inertia of the core, $V_{\pi\nu}$ and $V_{\pi\pi}$ represent the effective proton–neutron and proton–proton interaction strengths, respectively, and n is the number of particle–hole pair combinations for a given configuration [46]. The first term corresponds to core rotation, the second term arises from the repulsive interaction between proton holes and neutron particles, and the third term represents the attractive interaction between proton holes.

The total angular momentum is obtained by minimizing the energy with respect to the shears angle,

$$\frac{dE(I)}{d\theta} = 0, \quad (13)$$

which leads to

$$I = aj + 2j \cos \theta + \frac{1.5 \mathfrak{J}^{(2)} V_{\pi\nu} \cos \theta}{j} - \frac{6 \mathfrak{J}^{(2)} V_{\pi\pi} \cos 2\theta \cos \theta}{nj}, \quad (14)$$

where $a = j_\nu / j_\pi$ and $j = j_\pi$. The first two terms, $aj + 2j \cos \theta$, represent the contribution from the pure shears mechanism.

At the bandhead ($\theta = 90^\circ$), the angular momentum reduces to $I = aj = j_\nu$, indicating the alignment of the neutron angular momentum. As the shears gradually close with increasing spin, the angular momentum builds up and reaches the maximum shears angular momentum I_{sh}^{\max} at full closure ($\theta = 0^\circ$).

The angular frequency associated with the shears mechanism, ω_{sh} , is given by

$$\omega_{sh} = \left(\frac{dE_{sh}}{d\theta} \right) / \left(\frac{dI_{sh}}{d\theta} \right) = \frac{1.5 V_{\pi\nu} \cos \theta}{j} - \frac{6 V_{\pi\pi} \cos 2\theta \cos \theta}{nj}. \quad (15)$$

The total angular momentum can thus be written as

$$I = I_{sh} + \mathfrak{J}^{(2)} \omega_{sh}. \quad (16)$$

At full shears closure ($\theta = 0^\circ$),

$$\mathfrak{J}^{(2)} \omega_{sh}|_{\theta=0} = I^{\max} - I_{sh}^{\max}, \quad (17)$$

which gives

$$\omega_{sh}|_{\theta=0} = \frac{1.5 V_{\pi\nu}}{j} - \frac{6 V_{\pi\pi}}{nj}. \quad (18)$$

The total rotational frequency is expressed as

$$\omega_{rot} = \omega + \omega_{sh}. \quad (19)$$

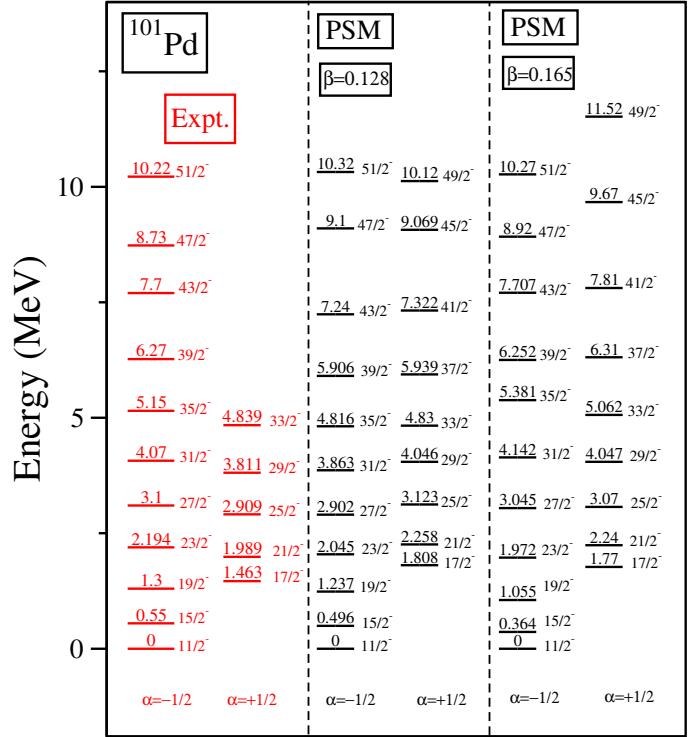


FIG. 2. (Color online) Comparison of PSM calculated energies after configuration mixing with the corresponding available experimental data [24] for ^{101}Pd .

The reduced transition probability for the electric quadrupole transition is given as a function of the shears angle by

$$B(E2) = \frac{15}{32\pi} (eQ_{\text{eff}})^2 \sin^4 \theta, \quad (20)$$

where the effective quadrupole moment is

$$eQ_{\text{eff}} = e_\pi Q_\pi + \left(\frac{j_\pi}{j_\nu} \right)^2 e_\nu Q_\nu. \quad (21)$$

In the $A \approx 100$ mass region, the effective interaction strengths are typically $V_{\pi\nu} \approx 1.2$ MeV and $V_{\pi\pi} \approx 0.2$ MeV.

IV. RESULTS AND DISCUSSION

The extended PSM calculations have been performed for ten nuclides of $^{101,103,107,109,111}\text{Pd}$ and $^{103,105,107,109,111}\text{Cd}$. We have chosen these nuclei as some of the them have well established MR and AMR band structures and for others predictions are made for the possible existence of these modes. It may be noted that ^{105}Pd is missing from the studied Pladium series as for this system, wobbling bands have been identified and has been studied using the triaxial projected shell model approach [49]. The deformation values used to obtain the Nilsson configurations are listed in Table I. These values have been adopted from the earlier investigations on the studied nuclei [20, 21, 25, 26, 38–45]. Table I also provides the

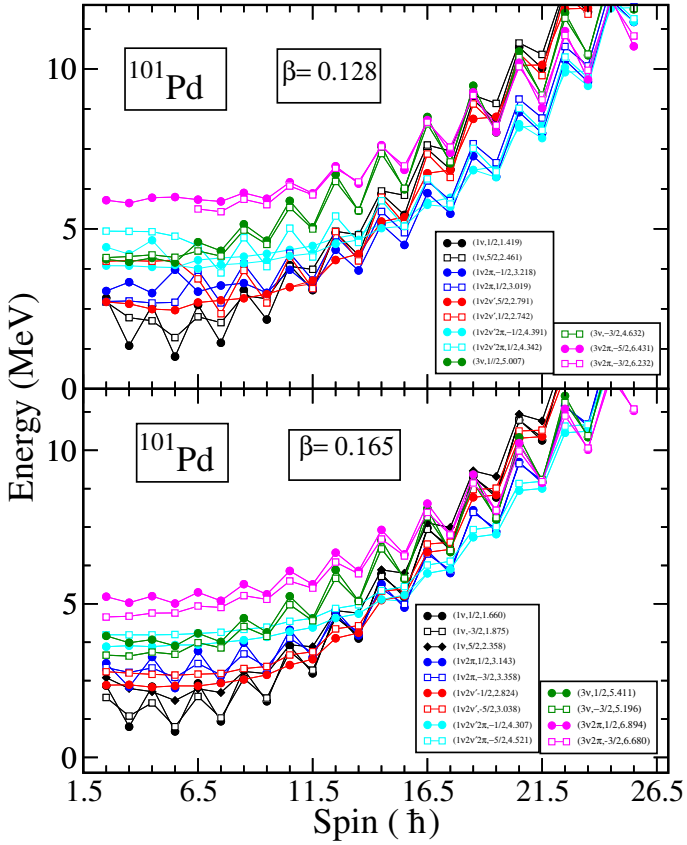


FIG. 3. (Color online) Angular-momentum projected energies are shown before diagonalization of the shell model Hamiltonian for ^{101}Pd .

pairing gaps obtained by solving the BCS equations with the strength parameters of the pairing interaction given in Eq. (6). In the following subsections, we discuss the results obtained for excitation energy, aligned angular-momentum and transition probabilities.

A. Excitation Energy

In this subsection, a detailed comparison of the PSM calculated excitation energies with the available data shall be made, and the results will be discussed individually for each nucleus.

The high-spin states of ^{101}Pd were studied using the in-beam γ -ray spectroscopic method [41]. The $\alpha = -1/2$ signature branch of the negative parity band based on $1/2^-$ [550] Nilsson configuration was extended up to spin, $I=43/2^-$. The $\alpha = +1/2$ branch of the band was also observed in this work up to $I=33/2^-$. The cranked shell model (CSM) analysis was performed and it was shown that the first observed bandcrossing at $\hbar\omega = 0.45\text{MeV}$ can be associated with the alignment of two-protons in $1g_{9/2}$. In a subsequent work [23], the negative parity band in ^{101}Pd was extended up to $I=51/2^-$ and the band structure was interpreted as an AMR band following the SCM analysis for this system. It was demonstrated that rotational properties of the band can be described using the

shears mechanism with neutrons aligned along the rotational axis, and the proton pair in the time-reversed orbits aligning towards the rotational axis with increasing spin.

The PSM calculations for ^{101}Pd have been performed with two sets deformation parameters, listed in Table I. The lower value of deformation has been adopted from the standard mass table of ref. [38] and also used in the number conserved CSM calculations [25]. The higher deformation value has been employed from the total Routhian surface (TRS) studies on ^{101}Pd , obtained for higher rotational frequencies. We shall demonstrate in the following that lower deformation set reproduces the low-lying spectrum, whereas the higher deformation value is needed to describe the high-spin characteristics.

The PSM calculated energies with two sets of deformation values along with the observed energies are displayed in Fig. (2). It is evident from the figure that PSM results for $\alpha = -1/2$ branch with $\epsilon = 0.128$ are in good agreement with the data up to $I=27/2^-$ and above this spin value it is the second set with $\epsilon = 0.165$ that depicts a better agreement. It will be shown below that in order to reproduce the observed band-crossing features properly in ^{101}Pd , it is essential to employ the two sets of deformation parameters.

For the $\alpha = +1/2$ branch, a deviation of about 0.3 MeV is noted. This deviation is recognized from the lowest $I=17/2^-$ state of the $\alpha = +1/2$ structure. The reason for this overall shift in the energies of the $\alpha = +1/2$ component is not understood at this stage and more work needs to be performed. However, it needs to be pointed out that spin assignment for $\alpha = +1/2$ signature branch in the experimental work of ref. [41] is tentative.

To analyze the intrinsic structures of the bands, the band diagrams of ^{101}Pd are displayed in Fig. (3) for the two deformation sets. In the band diagram, the projected energy of each intrinsic configuration is depicted as a function of the angular-momentum. These projected bands, before the shell model diagonalization, have diabatic crossings and it is easy to decipher the nature of the bandcrossings. It is noted from the band diagrams that that the projected bands from $K=1/2$ and $-3/2$ configurations are almost degenerate for the low-spin states with both deformation values. It is expected that ground-state band will be composed of these two configurations. These states are crossed in the high-spin region by three-quasiparticle states, and the crossing features are different for the two sets. For the lower deformation value, shown in the upper panel of Fig. (3), the three quasiparticle state with aligned two-protons crosses at $I=27/2^-$ and becomes favoured in energy. In the case of larger deformation value, shown in the lower panel of Fig. (3), the one-quasiparticle and three-quasiparticle structures are almost degenerate for the spin states of $I=27/2^-, 31/2^-$ and $35/2^-$, and, therefore, the yrast band will be mixed for these states with the consequence that backbending is not expected. However, the five-quasiparticle state becomes favoured in energy at $I=47/2^-$ with larger deformation value, whereas for the lower deformation set, this crossing is delayed. This five-quasiparticle configuration has three neutrons in the $N=5$ shell and two-protons in the $N=4$ shell. It is noted that five-quasiparticle state with one-neutron in the $N=5$ shell, two-neutrons in the $N=4$ shell

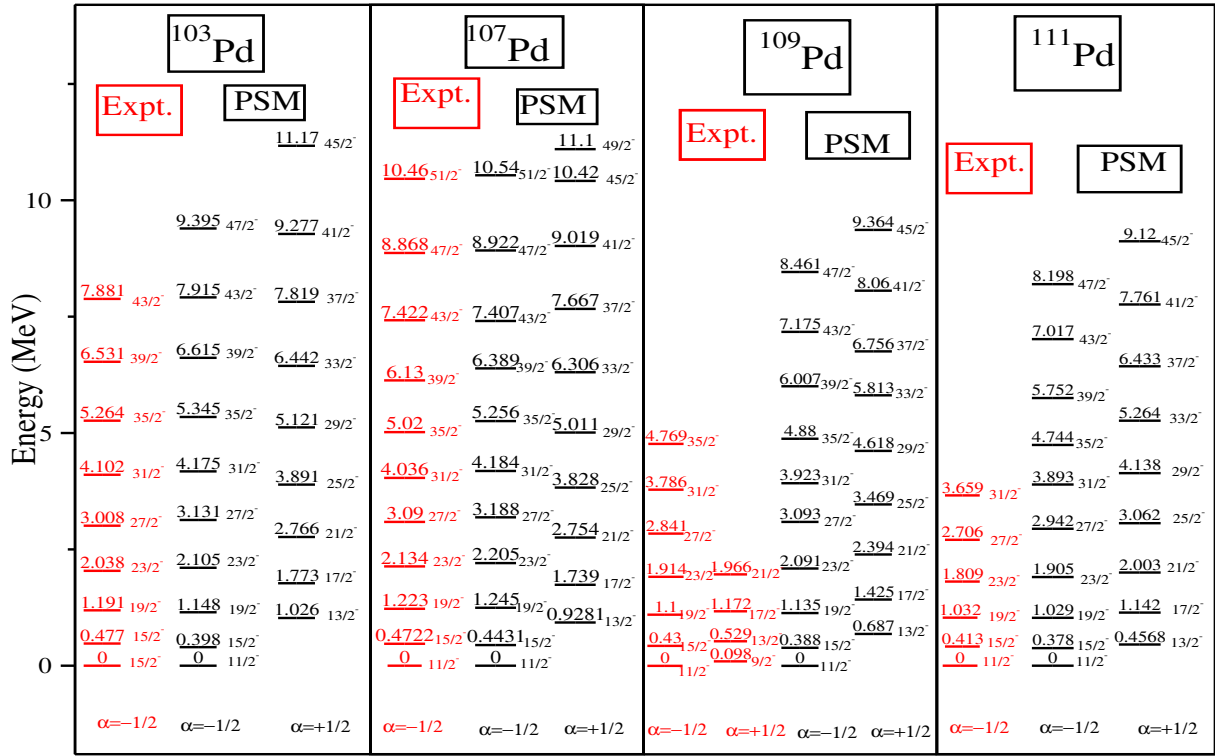


FIG. 4. (Color online) Comparison of PSM calculated energies after configuration mixing with the corresponding available experimental data [20, 26, 47] for $^{103,107-111}\text{Pd}$.

and two-protons in the N=4 shell is almost degenerate with the three-quasiparticle configuration for the intermediate spin states.

The crossing for the $\alpha = +1/2$ member occurs at an earlier spin value of $I=17/2^-$ for both deformation sets, and is due to the alignment of two-neutrons. However, it is noted that neutron- and proton-aligned configurations are very close in energy and it will be discussed later that bandcrossings are mixed.

The negative parity band structure in ^{103}Pd was established as the AMR band through the lifetime measurements [26]. It was observed that $B(E2)$ transitions drop with spin along the band, and also the ratio of moment-of-ratio to $B(E2)$ was found to be quite large. Theoretical calculations using covariant density functional and SCM approaches were shown to be good agreement with the experimental data [26]. However, the comparison of the bandcrossing frequencies exhibited discrepancies [26]. The calculations predicted almost simultaneous neutron and proton crossssings at $\hbar\omega = 0.48$ MeV and 0.50 MeV, respectively. The observed bandcrossings are noted to be at $\hbar\omega=0.55$ MeV and 0.64 MeV.

PSM calculated energies for the two signature branches of ^{103}Pd and the known experimental band for the $\alpha = -1/2$ are depicted in Fig. (4). The comparison of the $\alpha = -1/2$ component shows an overall good agreement. The deviation is noted to be about 100 keV for most of the spin states. The $\alpha = +1/2$ states have not been observed for this system, and PSM energies are provided in Fig. (4) for future comparisons.

The band diagram of ^{103}Pd , displayed in Fig. (5), reveals

that one-quasiparticle neutron configurations with $K=1/2$ and $-3/2$ are favoured for low-spin states, and the yrast-state band will have dominant contributions from these two configurations. It is noted from the figure that ground-state is crossed by a three-neutron state from the N=5 shell at $I=27/2^-$ for the $\alpha = -1/2$ signature branch, and up to $I=39/2^-$ this three-quasiparticle state remains the yrast configuration. The figure also shows that five-quasiparticle state having $K=1/2$, becomes yrast for $\alpha = -1/2$ at $I=43/2^-$ and above spin states. For the $\alpha = +1/2$ branch, the first bandcrossing is noted at $I=29/2^-$ and the second crossing is seen at $I=37/2^-$.

High-spin states in ^{107}Pd were studied using the heavy-ion fusion-evaporation reaction, ($^{18}\text{O} + ^{96}\text{Zr}$) [50], and the negative parity yrast band was established up to $I=51/2^-$. The comparison of the experimental energies with the PSM calculations for the $\alpha = -1/2$ branch, shown in Fig. (4), illustrates that PSM reproduces the data quite well. The corresponding band diagram in Fig. (5), depicts the intrinsic configurations of the bands in ^{107}Pd . It is noted from the figure that three projected bands from $K=1/2$, $-3/2$ and $5/2$ Nilsson configurations are almost degenerate from $I=5/2^-$ to $23/2^-$ and the ground-state band, obtained after shell model diagonalization, is expected to be a mixed state of the three configurations. The ground-state configuration is crossed by a three-neutron state at $I=27/2^-$, and a five quasiparticle state, composed of three-neutrons and two-protons, become yrast at $I=37/2^-$.

The neutron-rich ^{109}Pd and ^{111}Pd were probed through fission fragments following the fusion reaction [47] and the high-spin properties of the two isotopes were populated. For

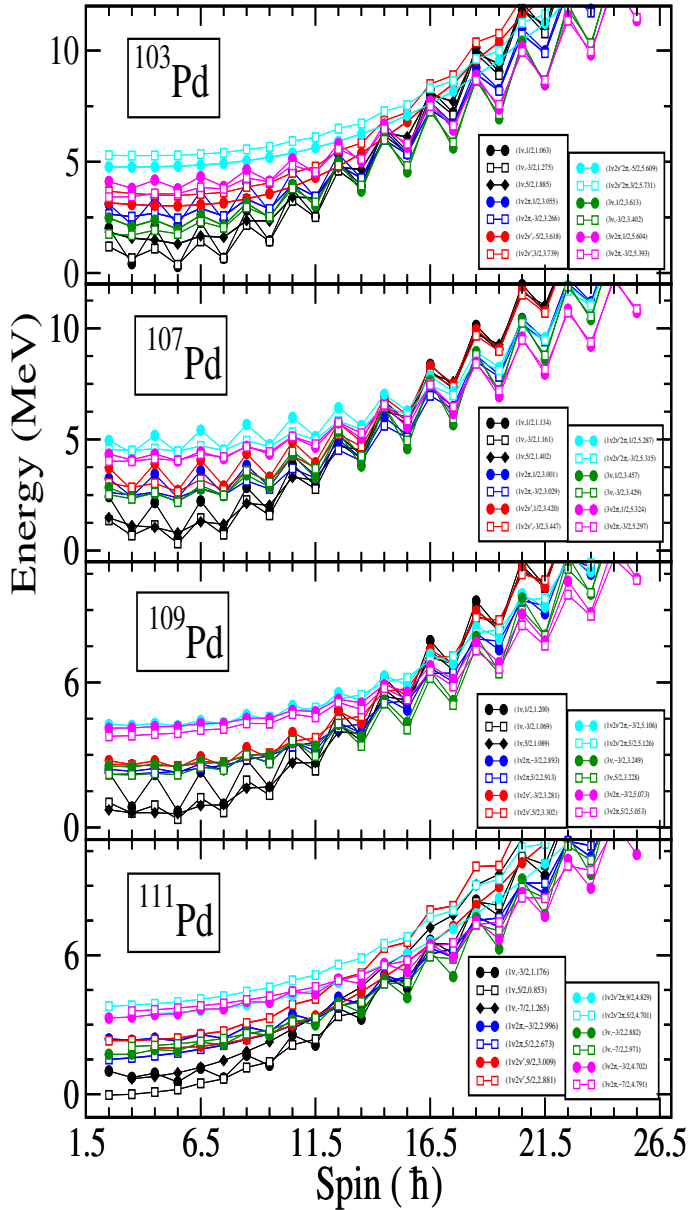


FIG. 5. (Color online) Angular-momentum projected energies are shown before diagonalization of the shell model Hamiltonian for $^{103,107-111}\text{Pd}$.

^{109}Pd , both signature branches of the yrast negative parity band were identified, whereas for ^{111}Pd only the favoured branch was populated in the experimental work [47]. These observed energies are compared with the PSM calculated energies in Fig. (4), and it is noted that PSM approach reproduces the data quite well. The band diagrams of the two isotopes, Fig. (5), reveal that the first bandcrossing is due to the alignment of two-neutrons in the $1h_{11/2}$ subshell, and the second crossing is due to further alignment of two-protons in the $1g_{9/2}$ subshell.

We shall now turn our discussion to the five Cadmium isotopes studied in the present work. ^{103}Cd has been investigated using the in-beam spectroscopic methods via the $^{72}\text{Ge}^{35}\text{Cl}$,

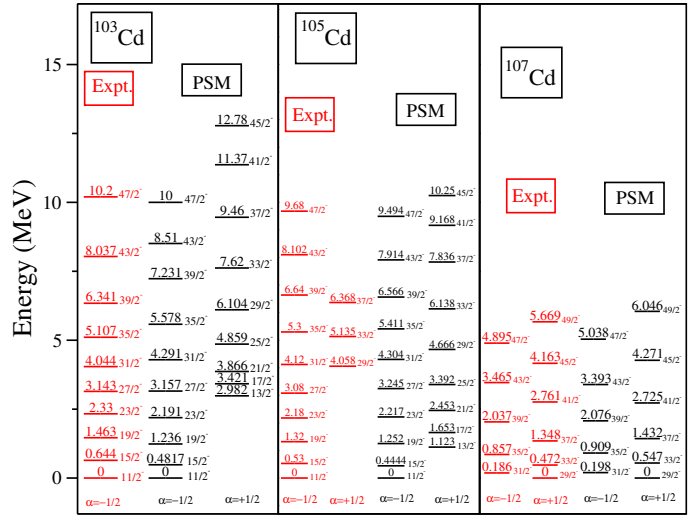


FIG. 6. (Color online) Comparison of PSM calculated energies after configuration mixing with the corresponding available experimental data [27, 44, 48] for $^{103-107}\text{Cd}$.

p3n) reaction [48] and the negative parity yrast band has been populated up to $I=47/2^-$. It is observed that this band depicts a regular rotational spectrum up to $I=39/2^-$, and above this spin irregular pattern of several parallel transitions are observed, indicating a possible change of level structure at high-spin. TRS calculations suggest that the collective prolate shape obtained at low rotational frequencies, transitions into a non-collective oblate shape at higher rotational frequencies [48]. The comparison of the calculated TPSM energies with the experimental energies is shown in Fig. (6) and it is noted that PSM approach reproduces the data well up to $I=31/2^-$, but above this spin large deviations are noted. The reason is quite clear as mean-field prolate deformation is kept fixed in the PSM calculations, and at higher spin shape transition to non-collective oblate shape is predicted by the TRS calculations [48]. This shape transition is neglected in the present version of the PSM approach, and will need implementation of the generator coordinate method [51-56]. The band diagram for ^{103}Cd , shown in Fig. (7), depicts a bandcrossing at $I=25/2^-$ due to the alignment of two-neutrons in the $N=4$ shell.

The negative parity yrast band in ^{105}Cd has been established to arise from the AMR mechanism [27]. The lifetime measurements for this system have been performed using the doppler shift attenuation technique. The deduced $B(E2)$ transitions beyond $I=23/2^-$ decrease with increasing spin, and the ratio of moment-of-inertia to $B(E2)$ has a large value as expected for an AMR structure. SCM calculations were performed and it has been shown that data is reproduced well with the AMR configuration for valence neutron particles and proton holes [27]. The PSM calculated energies are compared with the known experimental energies in Fig. (6) and it is evident that PSM reproduces the data reasonably well. There is a small deviation of about 0.1 MeV for the highest observed spin, $I=47/2^-$ in the $\alpha = -1/2$ signature branch. For the $\alpha = +1/2$, the deviation is much higher, and it needs to be added that the spin assignment for

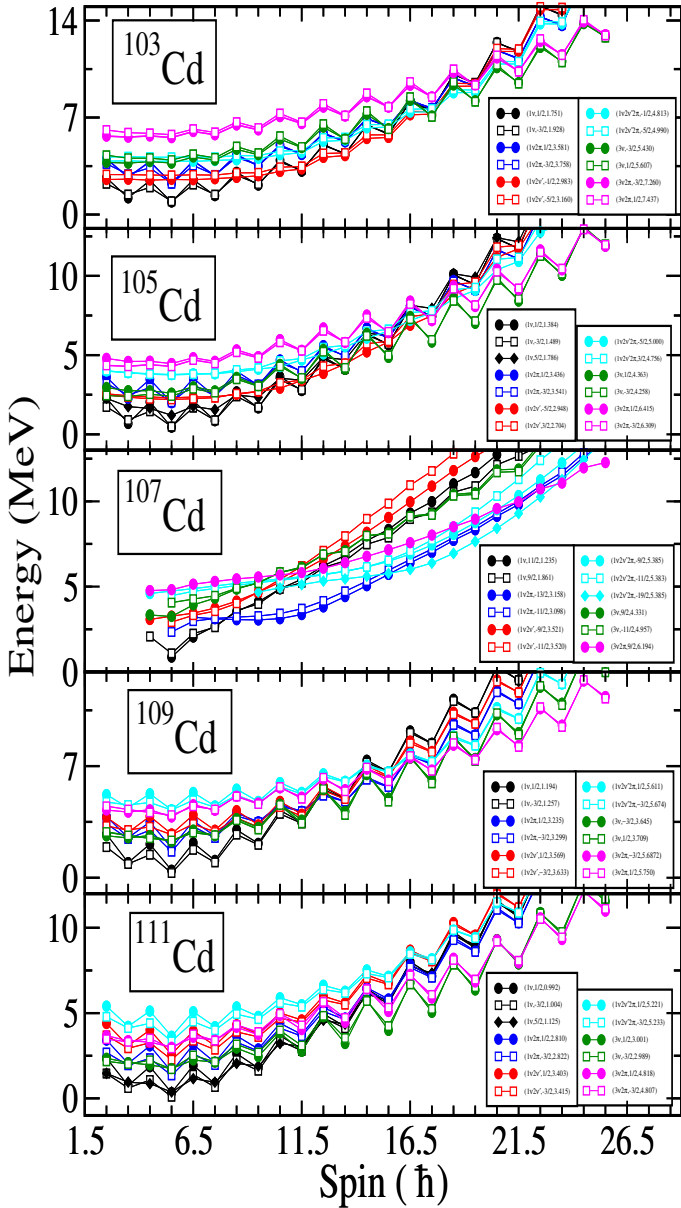


FIG. 7. (Color online) Angular-momentum projected energies are shown before diagonalization of the shell model Hamiltonian for $^{103-111}\text{Cd}$.

the $I=37/2^-$ is tentative [27]. The band diagram of ^{105}Cd , presented in Fig. (7), depicts an interesting crossing features. It is noted that $\alpha = +1/2$ one- quasiparticle state is crossed by a three-quasiparticle with two-neutrons in the $N=4$ shell at $I=21/2^-$. For the $\alpha = -1/2$, the crossing at $I=27/2^-$ is due to the alignment of two-neutrons in the $N=5$ shell. As a matter of fact, there are many three-quasiparticle states including one-neutron plus two-protons in the $N=4$ shell, which are close in energy and it is expected that the yrast band after $I=21/2^-$ will have a mixed configuration. There has been a detailed investigation regarding the nature of the bandcrossings in ^{105}Cd and it has been shown that for a lower deformation value, protons will align first, whereas for a larger deformation value the

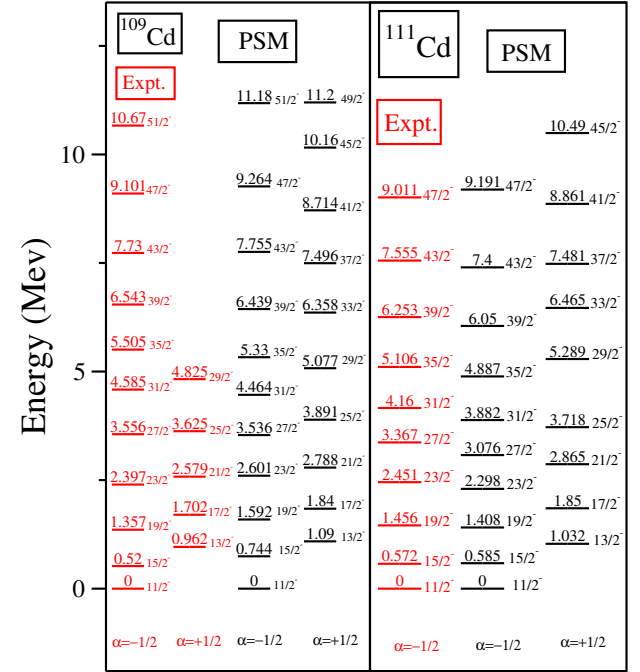


FIG. 8. (Color online) Comparison of PSM calculated energies after configuration mixing with the corresponding available experimental data [21, 22] for $^{109-111}\text{Cd}$.

two-neutron alignment will occur before the alignment of two protons [57]. It will be shown later, through the wavefunctions analysis, that the first bandcrossing in ^{105}Cd is due to a superposition of two-proton and two-neutron aligning configurations.

High-spin of the yrast negative parity band in ^{107}Cd were investigated using the $^{94}\text{Zr}(^{18}\text{O}, 5\text{n})$ reaction [44]. The $B(\text{M}1)$ probabilities were measured for five transitions in the high-spin region and they depict a decreasing trend with spin, which is a characteristic property of the MR band. Tilted axis cranking (TAC) analysis was also performed and it was shown that high-spin states beginning from $I=29/2^-$ have a five-quasiparticle structure. Further, a backbend is observed at $\hbar\omega = 0.72$ MeV and it was shown from the TAC calculations that it is due to the crossing of two five-quasiparticle configurations.

The PSM calculated energies for ^{107}Cd are compared with the known data in Fig. (6), and it is noted that PSM reproduces the data reasonably well. The major discrepancy of about 0.6 MeV is seen for the highest known spin value of $I=49/2^-$. The band diagram, plotted in Fig. (7), depicts interesting crossing features. The one-quasineutron band at low-spin is crossed by a three-quasiparticle band at $I=17/2^-$. The three-quasiparticle band is then crossed by a five-quasiparticle band at $I=31/2^-$. This five-quasiparticle structure has one-neutron in the $N=5$ shell, two-neutrons in the $N=4$ shell, and two-protons in the $N=4$ shell. It is also seen that this 5qp is crossed by another 5qp state with three-neutrons in the $N=5$ shell and two-protons in the $N=4$ shell at $I=47/2^-$. This crossing obtained in the PSM calculations is somewhat higher than observed in the

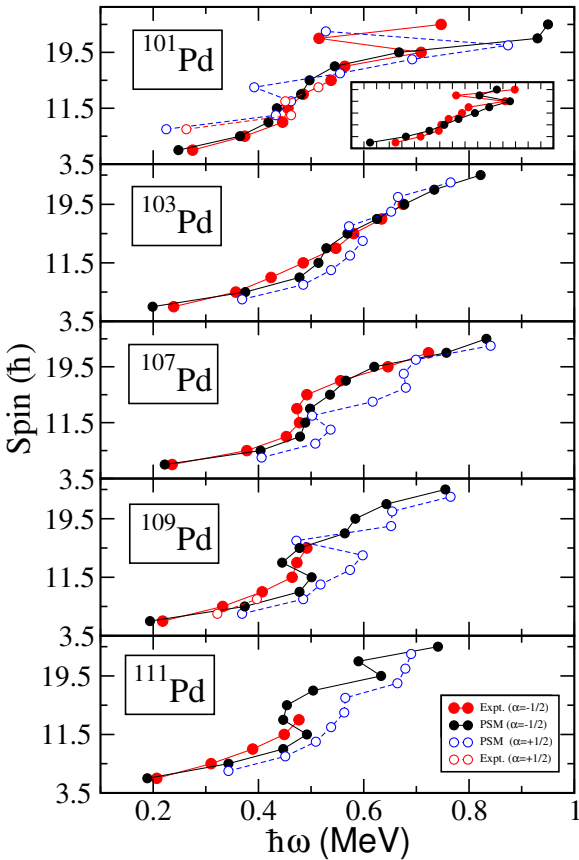


FIG. 9. (Color online) The PSM values of spin (\hbar) versus rotational frequency ($\hbar\omega = \frac{E(I)-E(I-2)}{2}$) are compared with experimental values for $^{101,103,107-111}\text{Pd}$.

data, which is around $I=41/2^-$. The reason for this discrepancy could be due to modification of the men-field potential at high-spin. Actually, TAC calculations predict a transition from oblate shape at high-spin in ^{107}Cd .

Shears bands, both AMR and MR, band structures have been observed in ^{109}Cd [21]. The yrast-band with one-neutron in low- Ω orbit, and two-neutrons in high- K time-reversed orbits, has been shown to have the AMR structure. The excited band with one-neutron and two-protons aligned along the rotational axis, has been demonstrated as having the MR characteristics. The experimental evidences of AMR and MR band structures have been corroborated with TAC and SCM theoretical calculations [21, 58]. The PSM calculated energies for ^{109}Cd are compared with the known experimental energies in Fig. (8). It is noted from the figure that PSM reproduces the data quite well for low- and medium spin states, however, for very high-spin states, deviations are noted. The band diagram for ^{109}Cd , displayed in Fig. (7), shows the alignment of two-neutrons in the $N=5$ shell at $I=23/2^-$, and then further alignment of two-protons in the $N=4$ shell at $I=39/2^-$.

Band structures in ^{111}Cd have been investigated in several

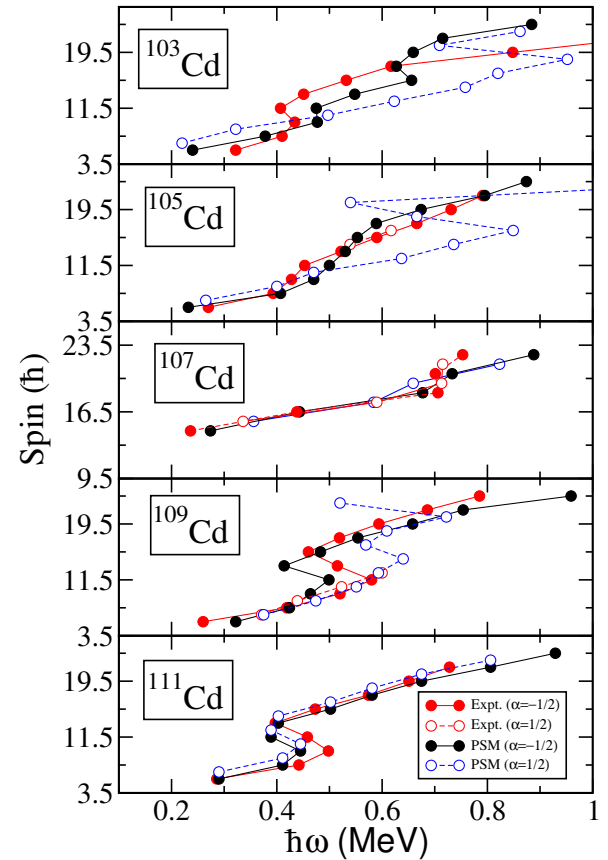


FIG. 10. (Color online) The PSM values of spin (\hbar) versus rotational frequency ($\hbar\omega = \frac{E(I)-E(I-2)}{2}$) are compared with experimental values for $^{103-111}\text{Cd}$.

experimental works [20, 45]. The predictions of the PSM calculations are compared with the known energies in Fig. (8), and it is evident from the figure that PSM reproduces the data quite well for the $\alpha = -1/2$ signature branch. The band diagram, shown in Fig. (7), depicts the bandcrossings at $I=23/2^-$ and $43/2^-$.

B. Spin versus rotational frequency

To investigate the bandcrossing phenomena in detail, the behaviour of angular-momentum, I , as a function of rotational frequency ($\hbar\omega$) is presented in Figs. (9) and (10) for the two isotopic chains of Pd- and Cd-nuclei. The plot in Fig. (9) for ^{101}Pd , obtained from the measured values, depicts an upbend at around $\hbar\omega = 0.45\text{MeV}$ and also a backbend at about $\hbar\omega = 0.6\text{ MeV}$. PSM calculations with $\beta = 0.128$ reproduces the upbend at $\hbar\omega = 0.45\text{MeV}$, and is due to the alignment of two-protons as is evident from the band diagram of Fig. (3). However, the backbending observed at $\hbar\omega = 0.6\text{ MeV}$ is not seen in the PSM with this deformation value. The PSM calcu-

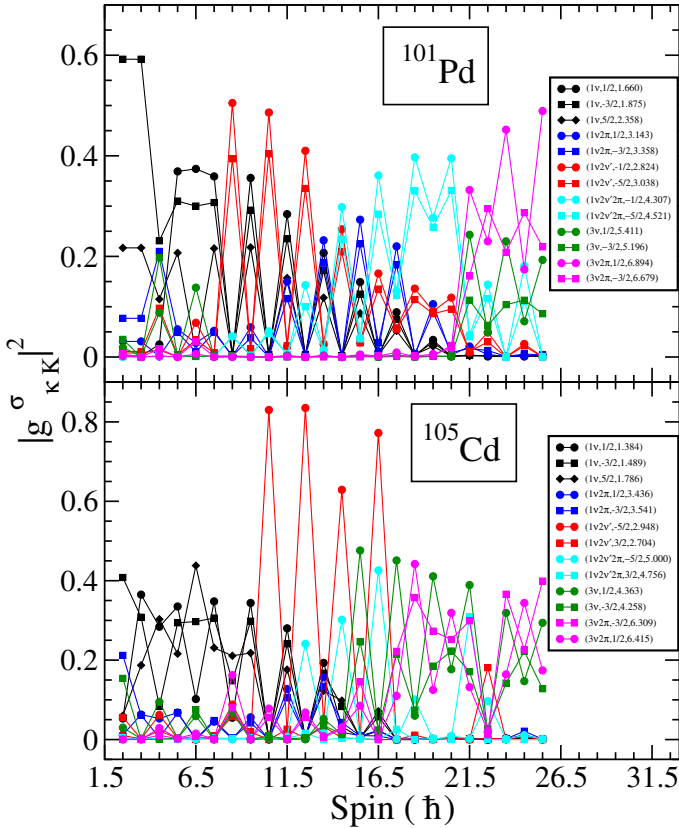


FIG. 11. (Color online) Wavefunction amplitudes of various projected K-configurations after diagonalization are plotted for ^{101}Pd and ^{105}Cd nuclides.

lations with the larger deformation value are shown in the inset of Fig. (9) and it is noted that upbend at $\hbar\omega = 0.45$ MeV is now absent, but the bandbend at $\hbar\omega = 0.6$ MeV is reproduced. We would like to mention that in the number-projected CSM calculations performed in ref. [25] with the smaller deformation value, the bandbend at $\hbar\omega = 0.6$ MeV is also absent. It can, therefore, be inferred from the bandcrossing analysis that ^{101}Pd undergoes a shape transition in the high-spin region.

For the $\alpha = +1/2$ signature component, the crossing features are somewhat different from the $\alpha = -1/2$ branch. A slight backbend is observed at about $\hbar\omega = 0.45$ MeV, and the PSM calculations also depict a backbend but with a weaker interaction between the ground-state and the aligned band as compared to the experimental data. The weaker interaction in the PSM calculations is deduced from the larger curvature of I verses $\hbar\omega$ curve.

The PSM calculated $\alpha = -1/2$ signature branch of ^{103}Pd in Fig. (9) depicts an upbend at around $\hbar\omega = 0.55$ MeV, whereas the $\alpha = +1/2$ branch shows a backbend at $\hbar\omega = 0.57$ MeV and an upbend at $\hbar\omega = 0.67$ MeV. The results corresponding to the experimental data also has an upbend at $\hbar\omega = 0.57$ MeV for the $\alpha = -1/2$ branch.

For ^{107}Pd , the observed backbend at about $\hbar\omega = 0.42$ MeV for $\alpha = -1/2$ branch is well reproduced by the PSM calculations. The PSM calculations show backbend at a slightly

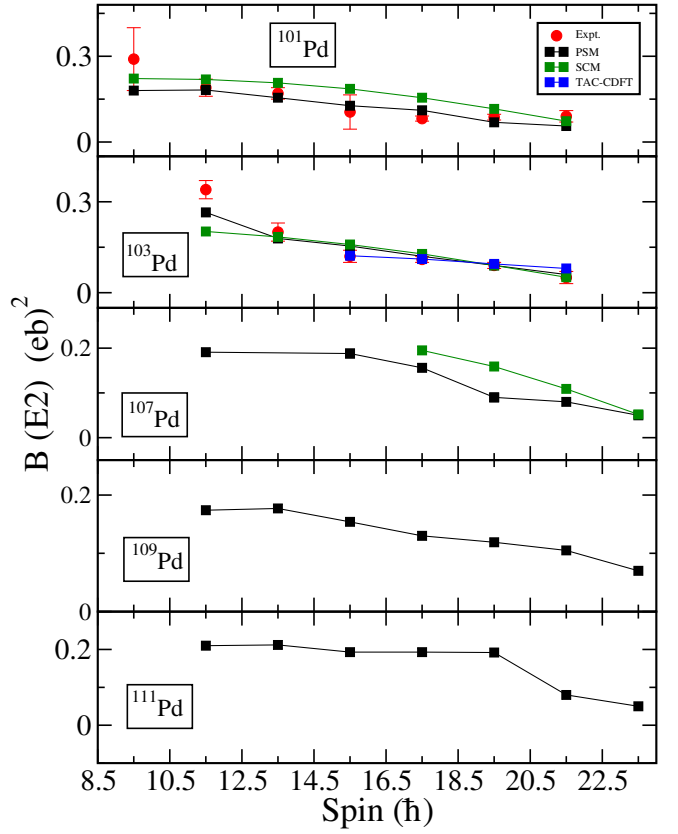


FIG. 12. (Color online) Comparison of $B(E2)$ transition probabilities ($e^2 b^2$) for $^{101,103,107-111}\text{Pd}$ isotopes.

higher rotational frequency for the $\alpha = +1/2$ signature partner branch, and another backbend at around $\hbar\omega = 0.68$ MeV. ^{109}Pd depicts a similar bandcrossing features as that of ^{107}Pd . In the case of ^{111}Pd , PSM calculations show a backbend at a similar rotational frequency as that ^{107}Pd and ^{109}Pd , but the experimental data is not available for the high-spin states to draw a comparison.

For the studied Cd-isotopes, the results of I verses $\hbar\omega$ are displayed in Fig. (10), and it is evident that PSM calculations are in good agreement with the experimental data. The backbending is observed for ^{103}Cd , ^{109}Cd and ^{111}Cd isotopes at about the same rotational frequency for the $\alpha = -1/2$ branch, and PSM approach reproduces this bandbending feature. For ^{105}Cd , an upbend is observed which is also reproduced reasonably well by the PSM calculations. ^{107}Cd depicts an upbend at a much higher rotational frequency of $\hbar\omega = 0.72$ MeV. For the $\alpha=+1/2$ branch, the backbending is observed in all the studied isotopes except for ^{107}Cd .

Further, the bandcrossings for odd-neutron Pd- and Cd-isotopes have a complex structure and cannot be solely attributed to either alignment of two-protons or two-neutrons. In order to illustrate the complex nature of the bandcrossings for the studied nuclides, the wavefunctions of two representative cases of ^{101}Pd and ^{105}Cd are depicted in Fig. (11). The displayed wavefunction amplitudes have been orthogonalized following the procedure outlined in Refs. [59, 60]. It is noted

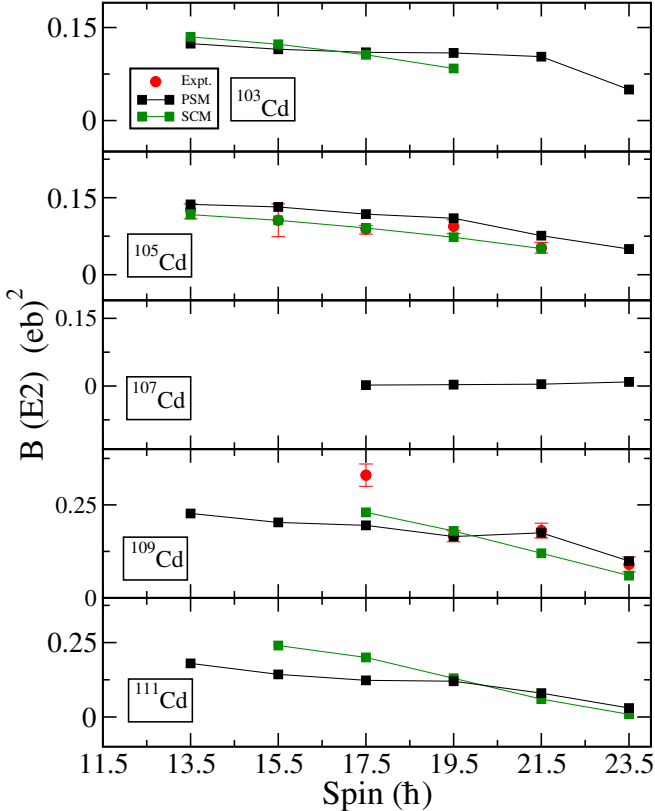


FIG. 13. (Color online) Comparison of $B(E2)$ transition probabilities ($c^2 b^2$) for $^{103-111}\text{Cd}$ isotopes.

from this figure that for ^{101}Pd , the yrast band is initially a one-quasiparticle state and is crossed by a three-quasiparticle state, having two-neutrons in the $N=4$ shell, at around $I=17/2^-$. Although this state is dominant, but there are many other configurations contributing significantly after the bandcrossing. For instance, the wavefunction has finite contribution from the three quasiparticle state having alignment of two-protons. In the high-spin region, the wavefunction is dominating by several five-quasiparticle configurations.

The wavefunction for ^{105}Cd , shown in the lower panel of Fig. (11), also depicts a complex structure after the bandcrossing at $I=19/2^-$. It is to be noted that after the alignment, the favoured and unfavoured signature branches have different structures. For the unfavoured branch, the crossing occurs first and has dominant three neutron configuration with one neutron in the $N=5$ shell and two aligning neutrons in the $N=4$ shell. In the case of favoured signature branch, the crossing occurs later, and after the crossing the dominant configurations is a three neutron state with all the neutrons in the $N=5$ shell.

C. Electric quadrupole transition probabilities

The important characteristic feature of the AMR structure is revealed through the lifetime measurements [22, 24, 26]. It has been shown using the SCM that $B(E2)$ transitions should

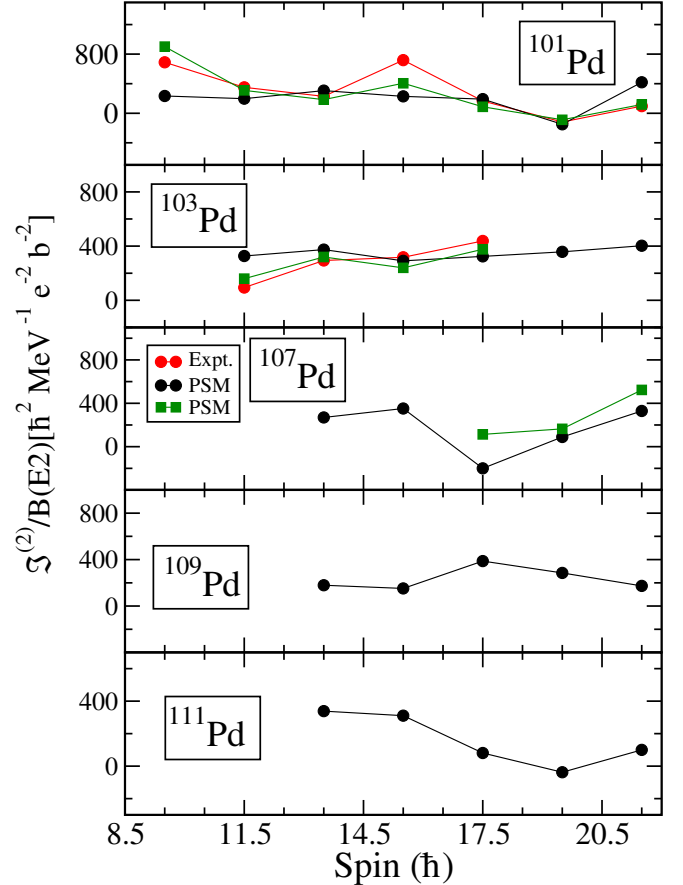


FIG. 14. (Color online) Comparison between experimental and calculated ratio of dynamic moment of inertia, $\mathcal{J}^{(2)} = \frac{4}{E_\gamma(I) - E_\gamma(I-2)}$, to $B(E2)$ for $^{101,103,107-111}\text{Pd}$ isotopes.

decrease with increasing spin along the band, and also ratio of moment-of-inertia to $B(E2)$ should have a large value. The latter feature is important as it distinguishes AMR from the phenomenon of terminating bands. For terminating bands, $B(E2)$ as well as moment-of-inertia decreases, but in the case of AMR only $B(E2)$ drops and the moment-of-inertia stays constant along the band. For the MR structures, the $B(M1)$ transitions depict a decreasing trend with spin, and the $B(E2)$ values are almost zero.

In Figs. (12) and (13), $B(E2)$ transition probabilities are depicted for the two isotopic chains of Palladium and Cadmium, respectively. The transition probabilities have been calculated with the expressions given in Section II and the effective charges of $e_p = 1.5e$ and $e_n = 0.5e$ for protons and neutrons, respectively. In most of the cases, it is noted that PSM calculated $B(E2)$ transitions decrease with spin. The detailed experimental transitions have been measured only for three nuclides of ^{101}Pd , ^{103}Pd and ^{105}Cd , and it is evident from the results that PSM approach provides a good description of the known data. It is to be noted that for ^{107}Cd , the $B(E2)$ transitions are almost zero as expected since the band has MR character. A few data points are also available for ^{109}Cd , and PSM values for the last two spin values are in good agreement

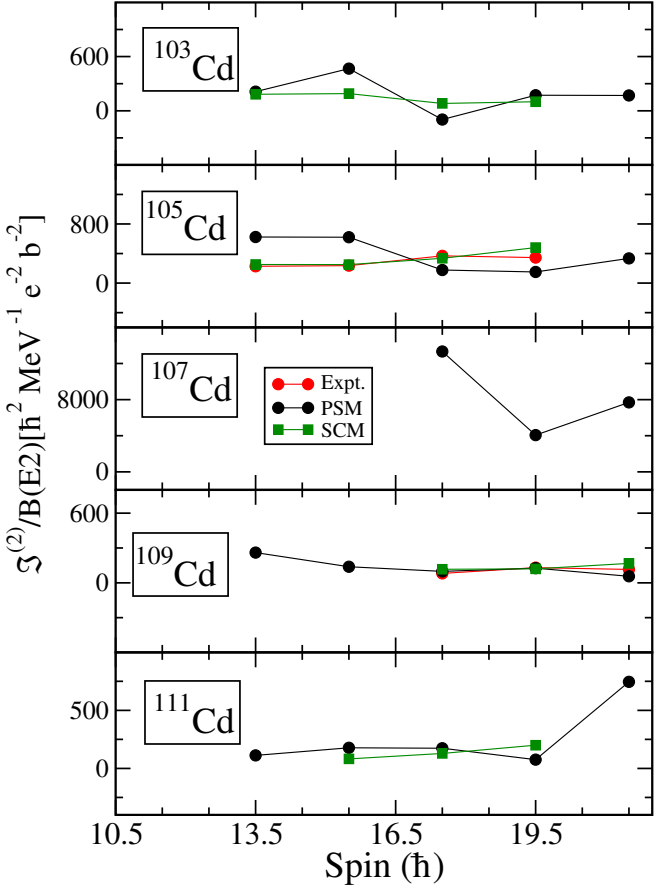


FIG. 15. (Color online) Comparison between experimental and calculated ratio of dynamic moment of inertia, $\mathcal{J}^{(2)} = \frac{4}{E_r(I) - E_r(I-2)}$, to $B(E2)$ for $^{103-111}\text{Cd}$ isotopes.

with the data. For the spin value of $I=35/2^-$, the known $B(E2)$ transition probability is higher than the PSM predicted value, and the reason for this discrepancy is not clear.

The ratios of moment-of-inertia to $B(E2)$ transitions are plotted in Figs. (14) and (15) for the two studied isotopic chains. The ratios in most of the cases remain constant, however, there are also some points where the ratios increase and decrease. These changes are due to the bandcrossings as moment of inertia being second derivative is very sensitive to any changes in the structure.

We have also evaluated the $B(M1)$ transitions with the effective g-factors of : $g_s(v) = -3.826 \times 0.70, g_l(v) = 0$ ($g_s(\pi) = 5.586 \times 0.70, g_l(\pi) = 1$) for neutron (protons), and are displayed in Fig. (16) for all the ten nuclides studied in the present work. As expected, $B(M1)$ transitions are almost zero for all the cases, except for ^{107}Cd , which has the MR character. It is evident from the figure that calculated $B(M1)$ transitions are in good agreement with the known transitions for this system.

For ^{109}Cd , one of the excited bands has been shown to have the MR properties [20, 21]. In the PSM calculations, the excited bands are quite mixed and it is difficult to identify the observed MR band structure. However, it is known that MR

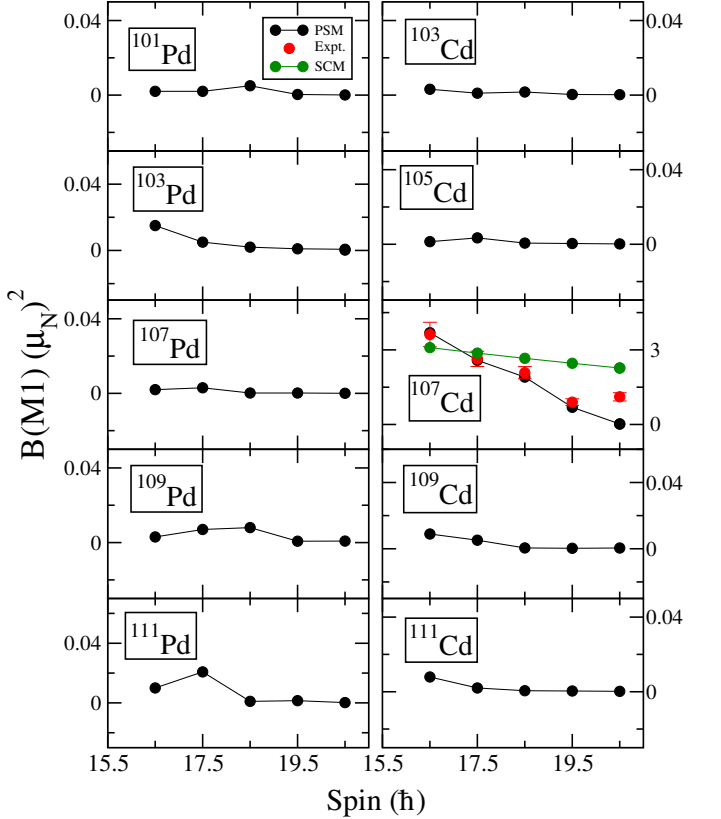


FIG. 16. (Color online) Comparison of $B(M1)$ transition probabilities for $^{101,103,107-111}\text{Pd}$ and $^{103-111}\text{Cd}$ isotopes.

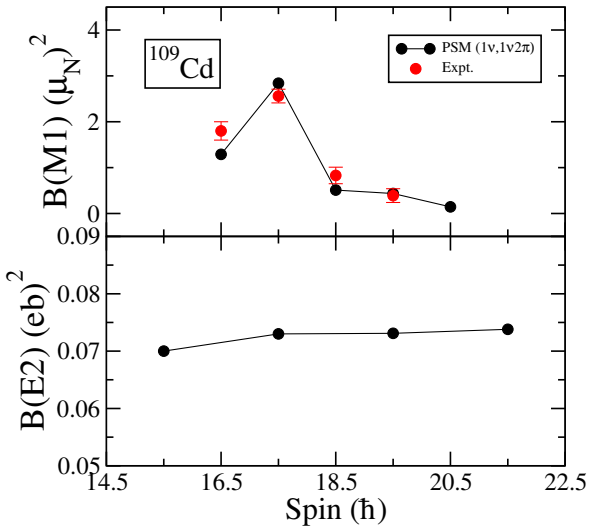


FIG. 17. (Color online) Comparison of $B(M1)$ and $B(E2)$ transition probabilities for ^{109}Cd isotope.

band has the $1v2\pi$ configuration and we have performed the PSM calculations with the basis space of $1v$ and $1v2\pi$ configurations only. The calculated $B(E2)$ and $B(M1)$ transitions are depicted in Fig. (17) and it is evident from the figure that $B(M1)$ transitions are in excellent agreement with the known

transitions. On the other hand, the BE(2) transitions are almost zero as expected for an MR band structure.

The electric quadrupole transition probabilities, B(E2), for the negative parity AMR bands in $^{103,105,109,111}\text{Cd}$ and $^{101,103,107}\text{Pd}$ isotopes have also been calculated using the semi-classical particle-rotor model. In these calculations, $\pi(g_{9/2})^{-4} \otimes v(h_{11/2})(d_{5/2}/g_{7/2})^2$ and $\pi(g_{9/2})^{-2} \otimes v(h_{11/2})(d_{5/2}/g_{7/2})^2$ quasiparticle configurations have been considered for Pd and Cd isotopes, respectively. Experimentally, the antimagnetic rotational character of the yrast negative parity band beyond alignment has been established conclusively in $^{105,109}\text{Cd}$ from lifetime measurements [21, 27]. The SCM calculation nicely reproduce the experimentally measured B(E2) values [22, 27]. The present calculations, shown in Fig. (13), are also found to be in agreement with the previously reported values. Although the band-head spins differ in the two Cd isotopes as they exhibit rotational alignment at different frequencies.

As already mentioned, the first AMR band in Pd-isotopes was identified in ^{101}Pd [23, 24] and unlike odd-Cd isotopes, here the lower spin part of the $v h_{11/2}$ band was proposed as the AMR band [24]. But, in a subsequent study, it was contradicted and the AMR character of $v h_{11/2}$ band was proposed within $31/2^-$ to $43/2^-$ spin range [61]. Later, AMR motion was also found in ^{103}Pd , where the measured B(E2) values were found in good agreement with SCM, as well as with TAC-CDFT theoretical estimates at higher spin [26]. However, the latest study on ^{103}Pd suggests that the angular momentum in this band arises from a combined contribution of antimagnetic rotation, collective rotation, and gradual neutron alignment [62]. The present SCM calculation, however, reasonably reproduce the experimentally deduced B(E2) values as depicted in Fig. (12).

It is interesting to note that the calculated B(E2) transitions of $^{103,111}\text{Cd}$ and ^{107}Pd are also found close to those measured experimentally for the well established AMR bands in $^{105,109}\text{Cd}$ and $^{101,103}\text{Pd}$ (see, Figs. (12) and (13)). Thus, the higher spin part, after alignment, of the negative parity yrast band in $^{103,111}\text{Cd}$ and ^{107}Pd are the possible candidates for AMR. The SCM results are also compared with those obtained from the newly developed extended PSM approach in this work, and it is evident from Figs. (12) and (13) that the results from the two approaches are in good agreement.

V. SUMMARY AND CONCLUSIONS

The main objective of the present work has been to develop a microscopic approach to investigate the properties of MR and AMR band structures. These structures have been observed in the vicinity of the closed shells and the characteristic feature of the AMR and MR structures is that they have a regular rotational spectrum, but the electric quadrupole transitions are quite weak as compared to a typical deformed nucleus. These new phenomena have been discussed using the shears mechanism with maximum contribution to angular-momentum originating from a few valence protons and neutrons, and the core contribution is very small.

In the present work, an extended PSM approach has been developed with quasiparticle excitations considered from two major oscillator shells. In the original PSM version, the excitations were restricted to one major shell only, although the vacuum configuration is generated from the three shells. It has been demonstrated in several studies that PSM approach provides an excellent description of the properties of the deformed nuclei in the neighbourhood of the yrast line [63–66]. The high-spin states along the yrast line are mostly generated by considering the quasiparticle excitations from the intruder orbital, which is a part of the one major shell chosen in the PSM basis space. However, to describe the non-yrast band structures, the quasiparticle excitations from the other major shells also needed to be included in the basis space. We have generalized the PSM approach to include the quasiparticle excitations from two major oscillator shells, and have also significantly enlarged the rank of the quasiparticle space. In most of the earlier studies, a maximum of three quasiparticle excitations were considered for odd-mass nuclei, and in the present study we have included up to five quasiparticle configurations in the basis space.

As a first application of the generalized PSM approach, we have investigated odd-mass Pd- and Cd-isotopes. These nuclei are situated in the vicinity of the $N=Z=50$ closed shell and in many of these nuclei, MR and AMR band structures have been observed. The high-spin states in these bands are mostly generated by the angular-momentum of the valence neutrons and protons. It has been demonstrated that PSM provided a reasonable description of most of the observed properties of the studied ten nuclides. The excitation energies for the favoured $\alpha = -1/2$ branch has been shown to be reproduced within 100 keV in almost all the cases. However, for the unfavored $\alpha = +1/2$ branch, some discrepancies have been noted. But the data is quite limited for this branch, and more data is needed to have a better assessment of the accuracy of the predicted values.

A detailed investigation of the bandcrossings has been performed of the studied isotopes. For ^{101}Pd , it has been shown that in order to reproduce the observed bandcrossings, one at $\hbar\omega = 0.45$ MeV and the other 0.6 MeV, two different deformation values are needed in the PSM calculations. The first crossing is due to the alignment of two-protons, and the second crossing is because of the further alignment of two-neutrons. In all other Pd-isotopes, the first crossing is due to the alignment of two-neutrons in the $N=5$ shell.

For ^{103}Cd , the first band crossing is due to the alignment of two-neutrons in the $N=4$ shell. In the case of ^{105}Cd , the first crossing in the $\alpha = -1/2$ branch is due to the alignment of two-neutrons in the $N=5$ shell, however, for the $\alpha = +1/2$ branch, it is due to the alignment of two-neutrons in the $N=4$ shell. For ^{107}Cd , an interesting crossing between two five quasiparticle configurations is noted. In the cases of ^{109}Cd and ^{111}Cd , the first crossing is due to the alignment of two-neutrons in the $N=5$ shell.

The most important characteristic feature for the existence of the MR and AMR band structures is revealed through the measurement of electromagnetic transitions. It has been shown using the phenomenological model that in the case of

AMR, the BE(2) transitions should drop with increasing spin and for the case of MR these should be vanishing. It has been shown that BE(2) transitions, indeed, drop for all the cases except for ^{107}Cd for which they are almost zero as it has an MR structure. On the other hand, BM(1) transitions are quite opposite with almost negligible for the AMR, and having the decreasing trend with spin for the MR case. We have also evaluated the ratios of $\mathcal{J}^{(2)}$ and B(E2) and it has been shown that they have almost constant values for most of the cases.

In conclusion, it has been shown that the extended PSM approach developed in the present work has provided a good description of the magnetic and antimagnetic rotational band structures observed in Pd- ad Cd -isotopes. This has been the first application of the generalized PSM approach, and in future we are planning to investigate the MR and MR band structure in the positive parity band structures of these nuclides,

and also explore the Pb-region, where these band structures were first identified.

ACKNOWLEDGEMENTS

N.N. acknowledges the Department of Science and Technology (Government of India) for the award of INSPIRE fellowship under Sanction No. DST/INSPIRE Fellowship/[IF200508]. S.C. gratefully acknowledges financial support from IEM, Kolkata for establishing the *Aage Bohr Laboratory for Nuclear Science* (BoNuS Lab) under the grant-in-aid project numbers: IEMT(S)/2025/R/04-G28; IEM(S)/2025/S/08-G63.

[1] A. Bohr and B. R. Mottelson, *Nuclear Structure* (World Scientific Publishing Company, 1998).

[2] P. Ring and P. Schuck, *The Nuclear Many-Body Problem* (Springer Berlin Heidelberg, 1980).

[3] S. Frauendorf, *Rev. Mod. Phys.* **73**, 463 (2001).

[4] S. Frauendorf, *Z. Phys. A* **358**, 163 (1997).

[5] M. Deleplanque, A. O. Macchiavelli, and I. Le, *Gammasphere Physics-Proceedings Of The Workshop* (World Scientific, 1996).

[6] R. M. Clark and A. O. Macchiavelli, *Annual Review of Nuclear and Particle Science* **50**, 1 (2000).

[7] S. Frauendorf, *Nuclear Physics A* **677**, 115 (2000).

[8] R. M. Clark, *Journal of Physics G: Nuclear and Particle Physics* **25**, 695 (1999).

[9] A. J. Simons, R. Wadsworth, D. G. Jenkins, R. M. Clark, M. Cromaz, M. A. Deleplanque, R. M. Diamond, P. Fallon, G. J. Lane, I. Y. Lee, A. O. Macchiavelli, F. S. Stephens, C. E. Svensson, K. Vetter, D. Ward, and S. Frauendorf, *Phys. Rev. Lett.* **91**, 162501 (2003).

[10] J. R. Cooper, R. Krücken, C. W. Beausang, J. R. Novak, A. Dewald, T. Klug, G. Kemper, P. von Brentano, M. P. Carpenter, R. V. F. Janssens, C. J. Lister, and I. Wiedenhöver, *Phys. Rev. Lett.* **87**, 132503 (2001).

[11] R. M. Clark, S. J. Asztalos, G. Baldsiefen, J. A. Becker, L. Bernstein, M. A. Deleplanque, R. M. Diamond, P. Fallon, I. M. Hibbert, H. Hübel, R. Krücken, I. Y. Lee, A. O. Macchiavelli, R. W. MacLeod, G. Schmid, F. S. Stephens, K. Vetter, R. Wadsworth, and S. Frauendorf, *Phys. Rev. Lett.* **78**, 1868 (1997).

[12] H. Hübel, *Progress in Particle and Nuclear Physics* **54**, 1 (2005).

[13] J. Peng, J. Meng, P. Ring, and S. Q. Zhang, *Phys. Rev. C* **78**, 024313 (2008).

[14] S. Frauendorf and Jie Meng, *Nucl. Phys. A* **617**, 131 (1997).

[15] C. M. Petrache, S. Frauendorf, B. F. Lv, A. Astier, E. Dupont, S. Guo, M. L. Liu, X. H. Zhou, K. L. Wang, P. T. Greenlees, H. Badran, D. M. Cox, T. Grahn, R. Julin, S. Juutinen, J. Konki, J. Pakarinen, P. Papadakis, J. Partanen, P. Rahkila, M. Sandzelius, J. Saren, C. Scholey, J. Sorri, S. Stolze, J. Uusitalo, B. Cederwall, O. Aktas, A. Ertoprak, H. Liu, I. Kuti, J. Timár, A. Tucholski, J. Srebrny, and C. Andreoiu, *Phys. Rev. C* **99**, 041301 (2019).

[16] P. W. Zhao, J. Peng, H. Z. Liang, P. Ring, and J. Meng, *Phys. Rev. Lett.* **107**, 122501 (2011).

[17] M. Wang, W. J. Sun, B. H. Sun, J. Li, L. H. Zhu, Y. Zheng, G. L. Zhang, L. C. He, W. W. Qu, F. Wang, T. F. Wang, C. Xiong, C. Y. He, G. S. Li, J. L. Wang, X. G. Wu, S. H. Yao, C. B. Li, H. W. Li, S. P. Hu, and J. J. Liu, *Eur. Phys. J. A* **56**, 31 (2020).

[18] J.-Q. Ma and Z.-H. Zhang, *Nuclear Physics A* **1016**, 122319 (2021).

[19] S. Kumar, S. Singh, B. Singh, Amita, and A. K. Jain, *Review of magnetic- and antimagnetic-rotational structures in nuclei* (2023), arXiv:2303.00499 [nucl-th].

[20] S. Juutinen, P. Šimeček, C. Fahlander, R. Julin, J. Kumpulainen, A. Lampinen, T. Lönnroth, A. Maj, S. Mitarai, D. Müller, J. Nyberg, M. Piiparinen, M. Sugawara, I. Thorslund, S. Törmänen, and A. Virtanen, *Nuclear Physics A* **577**, 727 (1994).

[21] C. J. Chiara, S. J. Asztalos, B. Busse, R. M. Clark, M. Cromaz, M. A. Deleplanque, R. M. Diamond, P. Fallon, D. B. Fossan, D. G. Jenkins, S. Juutinen, N. S. Kelsall, R. Krücken, G. J. Lane, I. Y. Lee, A. O. Macchiavelli, R. W. MacLeod, G. Schmid, J. M. Sears, J. F. Smith, F. S. Stephens, K. Vetter, R. Wadsworth, and S. Frauendorf, *Phys. Rev. C* **61**, 034318 (2000).

[22] C. Majumder, H. P. Sharma, S. Chakraborty, and S. S. Tiwary, *Int. Journal of Modern Phys. E* **27**, 1850034 (2018).

[23] M. Sugawara, T. Hayakawa, M. Oshima, Y. Toh, A. Osa, M. Matsuda, T. Shizuma, Y. Hatsukawa, H. Kusakari, T. Morikawa, Z. G. Gan, and T. Czosnyka, *Phys. Rev. C* **86**, 034326 (2012).

[24] M. Sugawara, T. Hayakawa, M. Oshima, Y. Toh, A. Osa, M. Matsuda, T. Shizuma, Y. Hatsukawa, H. Kusakari, T. Morikawa, Z. G. Gan, and T. Czosnyka, *Phys. Rev. C* **92**, 024309 (2015).

[25] Z.-H. Zhang, *Phys. Rev. C* **94**, 034305 (2016).

[26] A. Sharma, R. Raut, S. Muralithar, R. P. Singh, S. S. Bhattacharjee, S. Das, S. Samanta, S. S. Ghugre, R. Palit, S. Jehangir, N. Rather, G. H. Bhat, J. A. Sheikh, S. S. Tiwary, Neelam, P. V. Madhusudhana Rao, U. Garg, and S. K. Dhiman, *Phys. Rev. C* **103**, 024324 (2021).

[27] D. Choudhury, A. K. Jain, M. Patial, N. Gupta, P. Arumugam, A. Dhal, R. K. Sinha, L. Chaturvedi, P. K. Joshi, T. Trivedi, R. Palit, S. Kumar, R. Garg, S. Mandal, D. Negi, G. Mohanto, S. Muralithar, R. P. Singh, N. Madhavan, R. K. Bhowmik, and

S. C. Pancholi, *Phys. Rev. C* **82**, 061308 (2010).

[28] D. Choudhury, A. K. Jain, G. A. Kumar, S. Kumar, S. Singh, P. Singh, M. Sainath, T. Trivedi, J. Sethi, S. Saha, S. K. Jadav, B. S. Naidu, R. Palit, H. C. Jain, L. Chaturvedi, and S. C. Pancholi, *Phys. Rev. C* **87**, 034304 (2013).

[29] P. W. Zhao, J. Peng, H. Z. Liang, P. Ring, and J. Meng, *Phys. Rev. C* **85**, 054310 (2012).

[30] K. Hara and Y. Sun, *Int. J. Mod. Phys. E* **04**, 637 (1995).

[31] Y. Sun and J. Egido, *Nuclear Physics A* **580**, 1 (1994).

[32] R. Palit, J. Sheikh, Y. Sun, and H. Jain, *Nuclear Physics A* **686**, 141 (2001).

[33] D. Singh, A. Gupta, A. Kumar, C. Sharma, S. Singh, A. Bharti, S. Khosa, G. Bhat, and J. Sheikh, *Nuclear Physics A* **952**, 41 (2016).

[34] A. O. Macchiavelli, R. M. Clark, M. A. Deleplanque, R. M. Diamond, P. Fallon, I. Y. Lee, F. S. Stephens, and K. Vetter, *Phys. Rev. C* **58**, R621 (1998).

[35] A. O. Macchiavelli, R. M. Clark, P. Fallon, M. A. Deleplanque, R. M. Diamond, R. Krückken, I. Y. Lee, F. S. Stephens, S. Asztalos, and K. Vetter, *Phys. Rev. C* **57**, R1073 (1998).

[36] M. Sugawara, Y. Toh, M. Oshima, M. Koizumi, A. Osa, A. Kimura, Y. Hatsukawa, J. Goto, H. Kusakari, T. Morikawa, Y. H. Zhang, X. H. Zhou, Y. X. Guo, and M. L. Liu, *Phys. Rev. C* **79**, 064321 (2009).

[37] S. G. Nilsson, C. F. Tsang, A. Sobiczewski, Z. Szymański, S. Wycech, C. Gustafson, I.-L. Lamm, P. Möller, and B. Nilsson, *Nucl. Phys. A* **131**, 1 (1969).

[38] P. Moller, J. R. Nix, W. D. Myers, and W. J. Swiatecki, *Atomic Data and Nuclear Data Tables* **59**, 185 (1995).

[39] P. Möller, R. Bengtsson, B. G. Carlsson, P. Olivius, T. Ichikawa, H. Sagawa, and A. Iwamoto, *Atomic Data and Nuclear Data Tables* **94**, 758 (2008).

[40] S. Raman, C. Nestor, and P. Tikkanen, *Atomic Data and Nuclear Data Tables* **78**, 1 (2001).

[41] H. B. Zhou, X. H. Zhou, Y. H. Zhang, Y. Zheng, M. L. Liu, N. T. Zhang, L. Chen, S. T. Wang, G. S. Li, H. X. Wang, B. Ding, X. G. Lei, Y. X. Guo, G. X. Dong, F. R. Xu, M. Oshima, Y. Toh, M. Koizumi, A. Osa, and Y. Hatsukawa, *The European Physical Journal A* **47**, 107 (2011).

[42] E. A. Stefanova, S. Lalkovski, A. Korichi, T. Kutsarova, A. Lopez-Martens, F. R. Xu, H. L. Liu, S. Kisoyev, A. Minkova, D. Bazzacco, M. Bergström, A. Görgen, F. Hannachi, B. Herskind, H. Hübel, A. Jansen, T. L. Khoo, Z. Podolyák, and G. Schönwasser, *Phys. Rev. C* **86**, 044302 (2012).

[43] Z.-H. Zhang, P.-W. Zhao, J. Meng, J.-Y. Zeng, E.-G. Zhao, and S.-G. Zhou, *Phys. Rev. C* **87**, 054314 (2013).

[44] D. Choudhury, R. Palit, P. Singh, J. Sethi, S. Saha, S. Biswas, H. C. Jain, V. Nanal, R. G. Pillay, R. Donthi, S. K. Jadhav, B. S. Naidu, B. Maheshwari, A. K. Jain, S. C. Pancholi, R. P. Singh, S. Mukhopadhyay, D. C. Biswas, L. S. Danu, S. K. Tandel, L. Chaturvedi, K. Rojeeta Devi, and S. Singh, *Phys. Rev. C* **91**, 014318 (2015).

[45] P. H. Regan, J. S. Middleton, K. R. Pohl, J. E. Bush, P. E. Raines, D. P. Balamuth, S. M. Mullins, D. Ward, A. Galindo-Uribarri, V. P. Janzen, and S. Pilote, *Phys. Rev. C* **49**, 1885 (1994).

[46] S. Roy, S. Chattopadhyay, P. Datta, S. Pal, S. Bhattacharya, R. Bhowmik, A. Goswami, H. Jain, R. Kumar, S. Muralithar, D. Negi, R. Palit, and R. Singh, *Physics Letters B* **694**, 322 (2011).

[47] T. Kutsarova, A. Minkova, M.-G. Porquet, I. Deloncle, E. Gueorguieva, F. Azaiez, S. Bouneau, C. Bourgeois, J. Duprat, B. J. P. Gall, C. Gautherin, F. Hoellinger, R. Lucas, N. Schulz, H. Sergolle, T. Venkova, and A. Wilson, *Phys. Rev. C* **58**, 1966 (1998).

[48] A. Chakraborty, Krishchayan, S. Mukhopadhyay, S. Ray, S. N. Chintalapudi, S. S. Ghugre, N. S. Pattabiraman, A. K. Sinha, S. Sarkar, U. Garg, S. Zhu, and M. S. Sarkar, *Phys. Rev. C* **76**, 044327 (2007).

[49] A. Karmakar, P. Datta, N. Rather, S. Pal, R. Palit, A. Goswami, G. H. Bhat, J. A. Sheikh, S. Jehangir, S. Chattopadhyay, and S. Frauendorf, *Phys. Rev. C* **112**, 034323 (2025).

[50] K. R. Pohl, P. H. Regan, J. E. Bush, P. E. Raines, D. P. Balamuth, D. Ward, A. Galindo-Uribarri, V. P. Janzen, S. M. Mullins, and S. Pilote, *Phys. Rev. C* **53**, 2682 (1996).

[51] R. Balian and E. Brezin, *Nuovo Cim. B* **64**, 37 (1969).

[52] D. L. Hill and J. A. Wheeler, *Phys. Rev.* **89**, 1102 (1953).

[53] J. J. Griffin and J. A. Wheeler, *Phys. Rev.* **108**, 311 (1957).

[54] A. Valor, P.-H. Heenen, and P. Bonche, *Nucl. Phys. A* **671**, 145 (2000).

[55] R. Rodríguez-Guzmán, J. Egido, and L. Robledo, *Nucl. Phys. A* **709**, 201 (2002).

[56] J. Egido, *Phys. Scripta* **91** (2016).

[57] P. Regan, G. Dracoulis, G. Lane, P. Walker, S. Anderssen, A. Byrne, P. Davidson, T. Kibedi, A. Stuchbery, and K. Yeung, *Journal of Physics G: Nuclear and Particle Physics* **19**, L157 (1993).

[58] S. Roy and S. Chattopadhyay, *Phys. Rev. C* **83**, 024305 (2011).

[59] L.-J. Wang, F.-Q. Chen, and Y. Sun, *Phys. Lett. B* **808**, 135676 (2020).

[60] N. Nazir, S. Jehangir, S. P. Rouoof, G. H. Bhat, J. A. Sheikh, N. Rather, and M. A. Malik, *Phys. Rev. C* **108**, 044308 (2023).

[61] V. Singh, S. Sihotra, S. Roy, M. Kaur, S. Saha, J. Sethi, R. Palit, N. Singh, S. S. Malik, H. C. Jain, and D. Mehta, *Journal of Physics G: Nuclear and Particle Physics* **44**, 075105 (2017).

[62] A. Y. Deo, K. Yadav, Madhu, S. K. Tandel, and R. Kumar, *The European Physical Journal A* **57**, 126 (2021).

[63] B. Slathia, R. Devi, and S. Khosa, *Nuclear Physics A* **943**, 39 (2015).

[64] R. Chaudhary, N. Makhnatra, R. Devi, and S. Khosa, *Nuclear Physics A* **939**, 53 (2015).

[65] Y.-X. Liu, Y. Sun, X.-H. Zhou, Y.-H. Zhang, S.-Y. Yu, Y.-C. Yang, and H. Jin, *Nuclear Physics A* **858**, 11 (2011).

[66] Y. Sun, Y.-C. Yang, H. Jin, K. Kaneko, and S. Tazaki, *Phys. Rev. C* **85**, 054307 (2012).